



 Cite this: *Nanoscale*, 2021, **13**, 13108

## Continuous production of ultrathin organic–inorganic Ruddlesden–Popper perovskite nanoplatelets *via* a flow reactor†

 Gill M. Biesold,<sup>a</sup> Shuang Liang,<sup>a,b</sup> Brent K. Wagner,<sup>c</sup> Zhitao Kang<sup>\*a,c</sup> and Zhiqun Lin  <sup>\*a</sup>

Because of their enhanced quantum confinement, colloidal two-dimensional Ruddlesden–Popper (RP) perovskite nanosheets with a general formula  $L_2[ABX_3]_{n-1}BX_4$  stand as a promising narrow-wavelength blue-emitting nanomaterial. Despite ample studies on batch synthesis, for RP perovskites to be broadly applied, continuous synthetic routes are needed. Herein, we design and optimize a flow reactor to continuously produce high-quality  $n = 1$  RP perovskite nanoplatelets. The effects of antisolvent composition, reactor tube length, precursor solution injection rate, and antisolvent injection rate on the morphology and optical properties of the nanoplatelets are systematically examined. Our investigation suggests that flow reactors can be employed to synthesize high-quality  $L_2PbX_4$  perovskite nanoplatelets (*i.e.*,  $n = 1$ ) at rates greater than 8 times that of batch synthesis. Mass-produced perovskite nanoplatelets promise a variety of potential applications in optoelectronics, including light emitting diodes, photodetectors, and solar cells.

 Received 20th May 2021,  
 Accepted 10th July 2021  
 DOI: 10.1039/d1nr03239a

[rsc.li/nanoscale](http://rsc.li/nanoscale)

### Introduction

Due to their unique optoelectronic properties, colloidal semiconductor nanocrystals represent an exciting class of nanomaterials with a multitude of applications. Perovskite nanocrystals, with the general structure  $ABX_3$  (where A = monovalent cation (*e.g.*,  $CH_3NH_3^+$ ,  $CH_5N_2^+$ ,  $Cs^+$ , *etc.*), B = bivalent cation (*e.g.*,  $Pb^{2+}$ ,  $Sn^{2+}$ , *etc.*), and X = halide anion ( $Cl^-$ ,  $Br^-$ , or  $I^-$ )),<sup>1</sup> are particularly intriguing owing to their defect tolerance,<sup>2</sup> high photoluminescence quantum yield,<sup>3–6</sup> narrow emission bandwidth,<sup>7,8</sup> and direct and easily-tuneable bandgap.<sup>9</sup> These outstanding optoelectronic properties have led to a diverse array of applications, including solar cells,<sup>10–13</sup> light emitting diodes,<sup>14,15</sup> and photodetectors.<sup>16,17</sup> Two dimensional (2D) and quasi-2D organic–inorganic Ruddlesden–Popper (RP) perovskites have recently emerged as an intriguing subclass of perovskites. RP perovskites, with the general formula  $L_2[ABX_3]_{n-1}BX_4$  (where L = bulky alkylammonium cation (*e.g.*, phenylethylammonium (PEA),<sup>18</sup> butylammonium

(BA),<sup>19</sup> octylammonium (OA),<sup>20</sup> *etc.*), are formed when bulky organic spacer cations (*i.e.*, L) are placed at the monovalent A cation site.<sup>21,22</sup> A variety of L have been employed, including linear (*e.g.*, BA<sup>19</sup> and OA<sup>20</sup>), phenyl (*e.g.*, PEA<sup>18</sup> and 1-naphthylmethylammonium<sup>23</sup>), and bication (*e.g.*, diammonium butane<sup>24</sup> and diammonium octane<sup>24</sup>) architectures. As L is too large to fit within the  $ABX_3$  structure, it necessitates the formation of thin nanosheets. The thickness of RP perovskite is defined as  $n$ , which equals the number of layers of corner sharing octahedra. As  $n$  decreases, RP perovskites experience enhanced quantum confinement, which results in a dramatically blue-shifted emission<sup>20,25</sup> and an ultra-narrow full width at half max (FWHM).<sup>25</sup> The PLQY of perovskite NCs has, however, been found to decrease with decreasing thickness.<sup>20,26</sup> Notably, even with this decreased PLQY, the blue emission of  $(PEA)_2PbBr_4$  NCs is greater than that of Cl-containing perovskites (<10%).<sup>27</sup> The blue-shifted emission is of particular interest, as blue-emitting 3D perovskites (*e.g.*,  $ABCl_3$ ) are known to suffer from poor stability and possess sub-optimal photoluminescence (PL) characteristics.<sup>28–30</sup> Compared to 3D perovskites, RP perovskites possess a larger exciton binding energy due to low dielectric screening from the organic cation in conjunction with the confinement of electrons and holes within the 2D inorganic lattice.<sup>31–33</sup> Additionally, the hydrophobic nature of the ionically-bound L affords enhanced environmental stability to the 2D RP perovskites.<sup>32,34</sup> For example,  $(PEA)_2FA_{n-1}Sn_{n-1}I_{3n+1}$ -based solar cells maintained their full power conversion efficiency after

<sup>a</sup>School of Materials Science and Engineering, Georgia Institute of Technology, Atlanta, GA 30332, USA. E-mail: zhiqun.lin@mse.gatech.edu

<sup>b</sup>School of Chemical and Biomolecular Engineering, Georgia Institute of Technology, Atlanta, Georgia 30332, USA

<sup>c</sup>Georgia Tech Research Institute, Georgia Institute of Technology, Atlanta, Georgia 30332, USA. E-mail: Zhitao.kang@gttri.gatech.edu

†Electronic supplementary information (ESI) available. See DOI: 10.1039/d1nr03239a

over 100 h in air without encapsulation.<sup>35</sup> As such, 2D RP perovskites have been implemented for a diverse set of optoelectronic applications, including solar cells,<sup>36,37</sup> LEDs,<sup>38,39</sup> and photodetectors.<sup>40–42</sup>

While perovskites have demonstrated great promise for numerous applications, currently perovskite nanocrystals (NCs) are often created *via* batch synthetic techniques such as ligand-assisted reprecipitation (LARP)<sup>43</sup> and hot injection.<sup>44</sup> For perovskite NCs to reach their potential for widespread use, large-scale continuous production is highly desirable.<sup>45,46</sup> Successes in the use of flow reactors for the continuous production of a variety of other semiconductor NCs<sup>47,48</sup> have spurred some study into the use of flow reactors to synthesize 3D perovskite NCs. Recently, microfluidic flow systems have been used to probe the formation mechanisms of CsPbX<sub>3</sub><sup>49–51</sup> and FAPbX<sub>3</sub><sup>52</sup> NCs. In these studies, precursor solutions were isolated into droplets within an inert oil medium, which enabled complete mixing within a confined area. Using these microfluidic droplets, crystal growth for lead halide perovskites was shown to be complete within seconds of precursor mixing.<sup>51</sup> A Couette–Taylor flow system was also utilized to produce Cs<sub>4</sub>PbBr<sub>6</sub> NCs.<sup>53</sup> In this study, a precursor solution was combined with an antisolvent within the flow created between two spinning concentric cylinders.<sup>53</sup> This Couette–Taylor flow system was found to yield NCs with narrow FWHM and high photoluminescence quantum yield (PLQY) compared to those synthesized *via* conventional batch LARP approach. Notably, conventional flow reactor systems have also been explored. MAPbX<sub>3</sub> NCs were produced by continuously flowing two precursor solutions together.<sup>47</sup> The resulting NCs were, however, only stable for up to an hour in their native solvent. A PTFE microreactor was used to continuously create CsPbX<sub>3</sub> NCs. This strategy was able to create NCs with emission spanning 750–700 nm, yet required the use of a convection micromixer and elevated temperature.<sup>54</sup> A 3D printed nozzle was incorporated into a flow reactor to enhance mixing and craft MAPbX<sub>3</sub> NCs.<sup>55</sup> Interestingly, as demonstrated by both experimental and simulation results, by adding the precursor solution into the antisolvent through a narrowed 3D-printed nozzle, crystallization was improved, which in turn enhanced the PL properties of the NCs.<sup>55</sup>

Herein, we report the continuous manufacturing of high-quality (as defined by PLQY, FWHM, and emission peak position comparable to those previously reported) 2D RP perovskite NCs (*i.e.*, (PEA)<sub>2</sub>PbX<sub>4</sub> nanoplatelets (NPLs); X = Br and I; *n* = 1) *via* a house-built flow reactor. To our knowledge, no previous study has reported the continuous production of 2D RP NPLs. It is noteworthy that our flow reactor is able to produce NCs at rates over 15 times that previously reported.<sup>55</sup> Additionally, the relatively simple construction enables its widespread use without specialized equipment, unlike reactors that need relatively complex Couette–Taylor<sup>53</sup> or convection micromixer<sup>54</sup> apparatus. Furthermore, our flow reactor utilizes only two liquids, that is, the precursor solution and the antisolvent. This stands in sharp contrast to microfluidic platforms that necessitate the use of a third immiscible solvent as

the media to separate reactor droplets.<sup>49–52</sup> It is also notable that by introducing only two liquids, our flow reactor products can be used directly after synthesis, thereby dispensing with the need for removal of the third immiscible solvent, which is important for future industrial production. The effects of antisolvent composition, reactor tube length (*l*), antisolvent flowrate (*Q*<sub>anti</sub>), and precursor solution flowrate (*Q*<sub>precursor</sub>) on the PL properties (*i.e.*, PLQY, FWHM of emission, emission peak position, absorbance, *etc.*) and morphology of (PEA)<sub>2</sub>PbX<sub>4</sub> NPLs produced by flow reactor were elucidated. The antisolvent composition was witnessed to exert the greatest influence on the PL properties of the as-synthesized NPLs, with increasing polarity of the solvents leading to a consistent drop in PLQY. Reactor tube length and *Q*<sub>precursor</sub> were also identified to impact PLQY, with shorter reactor tubes and lower *Q*<sub>precursor</sub> generally resulting in better optoelectronic properties. *Q*<sub>anti</sub> was not found to significantly affect the final NPLs. The optimized parameters yielded NPLs with absolute PLQYs of 18.5% for (PEA)<sub>2</sub>PbBr<sub>4</sub> and 1.5% for (PEA)<sub>2</sub>PbI<sub>4</sub>, which are comparable to those reported for LARP synthesis.<sup>20,40,56,57</sup> 2D perovskites have been observed to possess lower PLQY than their 3D counterparts due to fast free exciton quenching *via* exciton–phonon coupling.<sup>58</sup> The flow reactor enables production rates of 0.1542 g h<sup>−1</sup> for (PEA)<sub>2</sub>PbBr<sub>4</sub>, which is at least eight times greater than that from batch synthesis. While flow reactors have been reported for 3D ABX<sub>3</sub> perovskites, to our knowledge, this is the first study on the continuous production of 2D RP perovskite NPLs. As such, it represents an important endeavour towards commercialization of this class of nanomaterials and offers a promise for the continuous production of other layered perovskites.

## Results and discussion

Fig. 1a and b depict the chemical structures of 3D ABX<sub>3</sub> and 2D L<sub>2</sub>PbX<sub>4</sub> perovskite, respectively. The bulky organic cation,

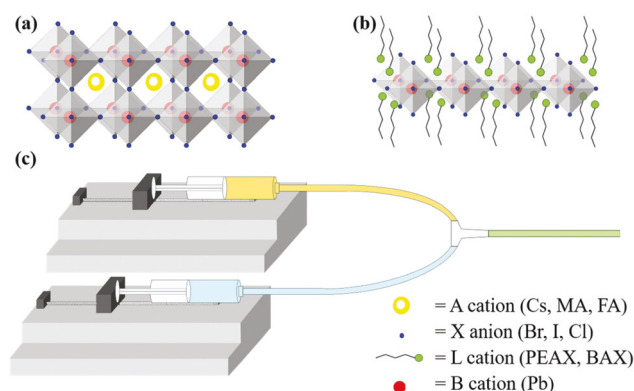


**Fig. 1** Schematic of (a) three-dimensional ABX<sub>3</sub> perovskite crystal structure, and (b) typical *n* = 1 L<sub>2</sub>PbX<sub>4</sub> Ruddlesden–Popper perovskite structure. (c) Schematic of in-house built flow reactor, where precursor solution and antisolvent are introduced separately *via* respective syringe pumps.

L, possesses a linear structure, where L cations can have diverse structures (*i.e.*, phenyl rings, branches, and other functionalities).<sup>18–20,23,24,32</sup> To facilitate the continuous synthesis of high-quality 2D (PEA)<sub>2</sub>PbX<sub>4</sub> perovskite NPLs, a custom flow reactor was built in house, as illustrated in Fig. 1c. Full details of its construction can be found in the Experimental section in the ESI.† Briefly, three PTFE tubes (3.2 mm inner diameter) were attached to a Y adaptor (3 mm orifice size). Two ends were fitted to syringe pumps and the other was left open. Precursor solution and antisolvent were then pumped through the tubing, combining in the Y adaptor and then the final product was collected at the end of the open tube. To optimize the synthesis of (PEA)<sub>2</sub>PbX<sub>4</sub> NPLs, four parameters were tuned in the flow reactor, that is, antisolvent composition, reactor tube length, antisolvent flowrate, and precursor solution flowrate.

### Investigation into the effect of antisolvent

The first parameter that was tailored was antisolvent composition. In a typical LARP synthesis of perovskite NPLs, a solution of perovskite precursors (*i.e.*, PEA<sub>X</sub> and PbX<sub>2</sub>) dissolved in a polar solvent (*e.g.*, dimethylformamide or dimethyl sulfoxide) is dropped into a vigorously stirred antisolvent that instantaneously triggers crystallization of the perovskite.<sup>43</sup> In contrast, the flow reactor uses a modified LARP technique, where instead of precursor solution being dropped into a stirring antisolvent, the precursor solution is pumped into a reactor tube while simultaneously pumping abundant antisolvent. The flow in the tube is then responsible for mixing the solution, rather than stirring in batch synthesis. In our study, following previously-reported LARP techniques, toluene, dichloromethane (DCM), and chlorobenzene were chosen as antisolvents in the flow reactor.<sup>59</sup> These three solvents were selected to isolate the effects of their structure and polarity on the final NPLs. Toluene and chlorobenzene are chemically identical except for the substitution of Cl for a methyl group. Comparison of NPLs synthesized with these two solvents renders evaluation of how the introduction of a single Cl group alters NPLs. Furthermore, dichloromethane was adopted as it offers a relatively higher polarity and the absence of a phenyl ring. To examine the effect of antisolvent composition, the antisolvent flowrate ( $Q_{\text{anti}}$ ) was set to a constant 1200 mL h<sup>-1</sup>, the reactor tube length fixed as 15 cm, and the precursor solution flowrate ( $Q_{\text{precursor}}$ ) varied from 5 to 30 mL h<sup>-1</sup>. Transmission electron microscopy (TEM) images of (PEA)<sub>2</sub>PbBr<sub>4</sub> NPLs produced with toluene antisolvent are shown in Fig. 2a–f. TEM images of the chlorobenzene and dichloromethane trials can be seen in Fig. S1a–f and S2a–f,† respectively. The NPL size distribution and average corner to corner length of NPLs made from both toluene and chlorobenzene can be seen in Fig. S3–4 (toluene) and S5–6 (chlorobenzene).† The average size and distribution of toluene NPLs was generally found to decrease with decreasing  $Q_{\text{precursor}}$ , which could be attributed to the relatively smaller amounts of precursors available for crystallization at low  $Q_{\text{precursor}}$  flowrates (Fig. S4†). Notably, this trend was not seen for the average size

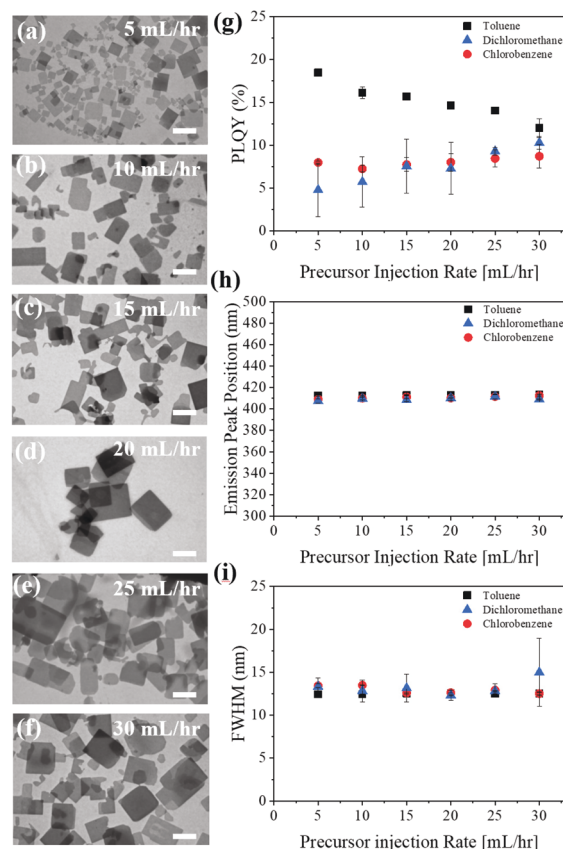


**Fig. 2** (a–f) TEM images of (PEA)<sub>2</sub>PbBr<sub>4</sub> nanoplatelets (NPLs) synthesized in the flow reactor with a reactor tube length of 15 cm, a toluene injection rate ( $Q_{\text{tol}}$ ) held constant at 1200 mL h<sup>-1</sup>, and  $Q_{\text{precursor}}$  ranging from 5–30 mL h<sup>-1</sup>, that is, (a) 5 mL h<sup>-1</sup>, (b) 10 mL h<sup>-1</sup>, (c) 15 mL h<sup>-1</sup>, (d) 20 mL h<sup>-1</sup>, (e) 25 mL h<sup>-1</sup>, and (f) 30 mL h<sup>-1</sup>, respectively. All scale bars = 2 μm. Effects of antisolvent composition and  $Q_{\text{precursor}}$  on (g) PLQY, (h) emission peak position, and (i) FWHM of emission of (PEA)<sub>2</sub>PbBr<sub>4</sub> NPLs.

and distribution of chlorobenzene crafted NPLs, which had a relatively constant average size of 2 μm (Fig. S6†). This could be due to the higher saturation limit of chlorobenzene, which would allow for more dissolution of the perovskite precursors.<sup>59</sup> We note that trends between morphology and  $Q_{\text{precursor}}$  are difficult to determine in DCM trials because of the potential decomposition of NPLs caused by DCM, as discussed below. As such, no NPL size measurements were taken for DCM samples. Interestingly, antisolvent composition was found to dramatically affect the quality of the produced (PEA)<sub>2</sub>PbBr<sub>4</sub> NPLs, as evidenced by the decreasing PLQY (Fig. 2g). NPLs crafted with solvents of a relative lower polarity were seen to exhibit higher PLQY. The relative polarities for toluene, chlorobenzene, and dichloromethane are 0.09, 0.188, and 0.309, respectively.<sup>59,60</sup> It is commonly reported that, because of their ionic nature, perovskite NCs can easily be degraded by polar solvents.<sup>2,61</sup> Thus, NPLs synthesized in relatively more polar solvents could be degraded, which would negatively impact their PLQY. This degradation can qualitatively be seen in differences of morphology of the NPLs. The

TEM images of NPLs formed from toluene (Fig. 2a–f) reveal more uniform NPLs compared to those of NPLs formed from chlorobenzene (Fig. S1a–f†) and DCM (Fig. S2a–f†). The samples made from DCM manifested clear degradation and often no NPL morphologies, which could be expected from its highest relative polarity. Antisolvent composition was found to have little effect on the emission wavelength or FWHM of NPLs (Fig. 2h and i), which is consistent with the fact that only  $n = 1$  (PEA)<sub>2</sub>PbBr<sub>4</sub> NPLs can form in the system, given the restrictive precursors.<sup>25</sup> The monolayer nature (and thus strong quantum confinement) of the NPLs ensured that the peak emission wavelength of all samples remained constant, as discussed later. This was further verified by absorbance and photoluminescence spectroscopy. Fig. S7–S9† clearly show the absorbance and emission from the NPLs remains unchanged regardless of the composition antisolvent.

### Influence of reactor tube length

After toluene was determined to be the optimal antisolvent, it was used to investigate the effect of reactor tube length on the optical properties of (PEA)<sub>2</sub>PbBr<sub>4</sub> NPLs. To this end, trials were run in the flow reactors with tube lengths of 15, 30 and 60 cm. For each tube length,  $Q_{\text{tol}}$  was fixed at 1200 mL h<sup>-1</sup> and  $Q_{\text{precursor}}$  ranged from 5–30 mL h<sup>-1</sup>. Reactor tube length was found to have little effect on the morphology of the as-synthesized NPLs. Representative TEM images of NPLs synthesized with different reactor tube lengths but otherwise identical conditions ( $Q_{\text{tol}} = 1200$  mL h<sup>-1</sup> and  $Q_{\text{precursor}} = 5$  mL h<sup>-1</sup>) are shown in Fig. 3a–c (TEM images for  $Q_{\text{precursor}}$  of 5–30 mL h<sup>-1</sup> for 15, 30, and 60 cm tube lengths are shown in Fig. 2a–f, S10 and S11,† respectively). The similarities of these TEM images signify that there is little effect from the reactor tube length. Reactor tube length was also found to exert a minimal effect on either FWHM or peak position (Fig. 3d–e). We note that consistent FWHM and peak position were also observed in both the toluene and chlorobenzene antisolvent trials. As noted above, a unique property of  $n = 1$  RP perovskite is its restricted ability to form only one product with a single, sharp emission peak.<sup>25</sup> Shorter reactor tube lengths were generally observed to result in a higher average PLQY (with the exception of  $Q_{\text{precursor}} = 30$  mL h<sup>-1</sup>, Fig. 3f). Notably, this inconsistency occurred at the highest  $Q_{\text{precursor}}$  level (30 mL h<sup>-1</sup>) and resulted in the lowest PLQY for each sample (between 10 and 12%). Thus, the inconsistency may be attributed to degradation from the relatively high concentration of polar DMF. For the 15 cm tube, a clear trend of increasing PLQY with decreasing  $Q_{\text{precursor}}$  can be observed, which is consistent with previous study.<sup>62</sup> This trend of increasing PLQY with decreasing  $Q_{\text{precursor}}$  was less pronounced for samples made with longer reactor tubes (30 and 60 cm). We hypothesize that this could be ascribed to longer tubes leading to an increase in residence time in the reactor tube. This increased residence time in turn could increase the interaction between DMF and the NPLs, thereby potentially degrading their structural integrity and decreasing PLQY. This residence time-induced degradation could obscure effects from increased  $Q_{\text{precursor}}$ , which

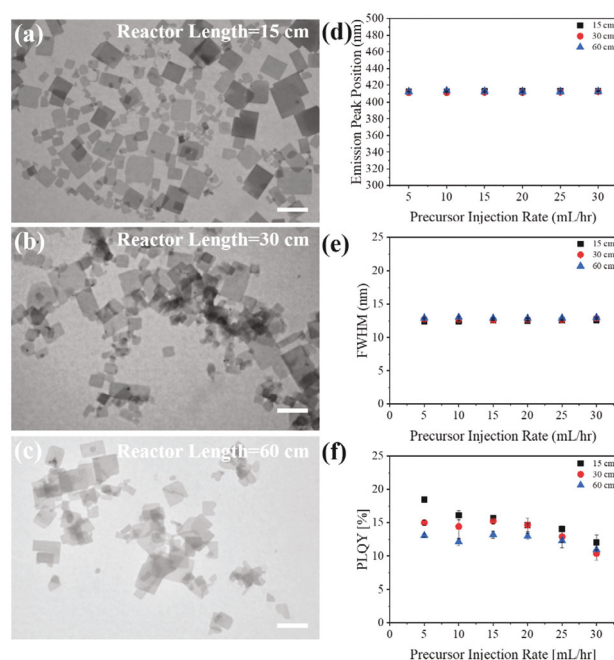


Fig. 3 TEM images of (PEA)<sub>2</sub>PbBr<sub>4</sub> NPLs produced in the flow reactor with (a) 15 cm, (b) 30 cm, (c) 60 cm reactor tubes and 1200 mL h<sup>-1</sup> toluene and 5 mL h<sup>-1</sup> precursor solution injection rates. All scale bars = 2 μm. Effects of reactor tube length (from 15 to 60 cm) and precursor injection rates (from 5 to 30 mL h<sup>-1</sup>) on (d) emission peak position, (e) FWHM, and (f) PLQY of (PEA)<sub>2</sub>PbBr<sub>4</sub> NPLs.

are more obvious in the shorter tube lengths where residence time-induced degradation is not as prevalent. Further study, including modelling of the complex fluid dynamics, is needed to better understand this phenomenon.

### Examination of precursor solution injection rate

Throughout both the antisolvent composition and reactor tube length trials, the effect of precursor solution injection rate ( $Q_{\text{precursor}}$ ) was also scrutinized. In both trials,  $Q_{\text{anti}}$  was kept constant at 1200 mL h<sup>-1</sup> and  $Q_{\text{precursor}}$  ranged from 5–30 mL h<sup>-1</sup>.  $Q_{\text{precursor}}$  was seen to impose a negligible impact on the peak position (Fig. 2h and 3d) of as prepared 2D perovskite NPLs (Fig. 2h and 3d). Additionally, the FWHM of all samples was found to be relatively unaffected by altering  $Q_{\text{precursor}}$  (Fig. 2i and 3e). The minor fluctuations from the DCM trial can be attributed to the high polarity of the solvent, as discussed above. The relative stability of both emission wavelength and FWHM are in agreement with the fact that, based on the precursors in the solution, any emissive crystals formed would necessarily have to be monolayer  $n = 1$  NPLs.  $Q_{\text{precursor}}$  was found to affect PLQY differently for each antisolvent. For DCM increasing  $Q_{\text{precursor}}$  resulted in an increase of PLQY (from ~5% to ~10%), for chlorobenzene altering  $Q_{\text{precursor}}$  had little impact on PLQY (stayed a relatively constant 8%), and for toluene decreasing  $Q_{\text{precursor}}$  led to an increase in PLQY (from ~10% to ~20%) (Fig. 3d). The trend of higher PLQY with increasing  $Q_{\text{precursor}}$  for the more polar solvents (DCM and

chlorobenzene) could be due to the relatively higher saturation concentrations of the perovskite precursor.<sup>59</sup> Because these relatively polar solvents encourage solvation of the precursor, a greater concentration of precursor is needed to enable the growth of quality crystals. For the samples synthesized with toluene (lowest polarity among all antisolvents), the consistently higher PLQY from lower  $Q_{\text{precursor}}$  is likely due to lower concentrations of DMF in the flow reactor. Because  $Q_{\text{tol}}$  is held constant, every increase of  $Q_{\text{precursor}}$  results in a relatively higher concentration of DMF in the reactor and final product solution. Final product solutions with relatively larger amounts of DMF impart a higher possibility of NPL degradation.<sup>63</sup> This is in good agreement with previous study which have shown that increasing the amount of precursor solution in conventional LARP methods rapidly decreases the PLQY of the resultant nanocrystals.<sup>62</sup> Additionally, lower  $Q_{\text{precursor}}$  could result in better mixing of the precursor with antisolvent due to the relatively higher ratio of antisolvent to precursor. This higher ratio could increase the likelihood of complete crystallization.

### Scrutiny of antisolvent flowrate

After the optimal antisolvent composition, reactor tube length, and  $Q_{\text{precursor}}$  were identified, the influence of  $Q_{\text{anti}}$  on  $(\text{PEA})_2\text{PbBr}_4$  NPLs was probed. For this trial, the previously optimized antisolvent composition (toluene), reactor tube length (15 cm), and  $Q_{\text{precursor}}$  ( $5 \text{ mL h}^{-1}$ ) were held constant while the toluene flowrate ( $Q_{\text{tol}}$ ) was varied from  $514$ – $1200 \text{ mL h}^{-1}$ . Altering  $Q_{\text{tol}}$  was seen to have little impact on the morphology of the as-synthesized NPLs. The TEM images of NPLs produced from the various  $Q_{\text{tol}}$  (Fig. 4a–e) display few differences, with the exception of the TEM image from the lowest  $Q_{\text{tol}}$  ( $514 \text{ mL h}^{-1}$ , Fig. 4e) which resulted in irregular NPLs with some structural degradation. This could be attributed to the relatively higher ratio of DMF:antisolvent for the lower  $Q_{\text{tol}}$  trial, which could degrade the as-formed NPLs *via* the presence of high-concentration polar solvent (*i.e.*, DMF). The particle size distribution and average corner to corner length and distribution of these NPLs are shown in Fig. S12 and S13.† Fig. S13† illustrates that NPLs made with the highest and lowest  $Q_{\text{tol}}$  resulted in NPLs with average sizes of with averages size of  $2 \pm 1 \mu\text{m}$  and  $4.5 \pm 3 \mu\text{m}$ , respectively. This trend of decreasing size and distribution with increasing  $Q_{\text{tol}}$  can be attributed to the enhanced mixing that occurs at higher flowrates, which is consistent with previous studies.<sup>64,65</sup> Changing  $Q_{\text{tol}}$  imposed little effect on PLQY, and FWHM, or peak position of NPLs (Fig. 4f–h). This can be ascribed to the fact that, though the flowrate of toluene was tuned over a wide range, the nature of the flow in the tube was unchanged. To confirm this, the Reynolds number ( $Re$ ) corresponding to the flow for each trial was calculated using the following equation:

$$Re = \frac{\rho QD}{\mu A}$$

where  $\rho$  is the density of the fluid,  $\mu$  is the dynamic viscosity of the fluid,  $A$  is the cross-sectional area of the tube, and  $D$  is the

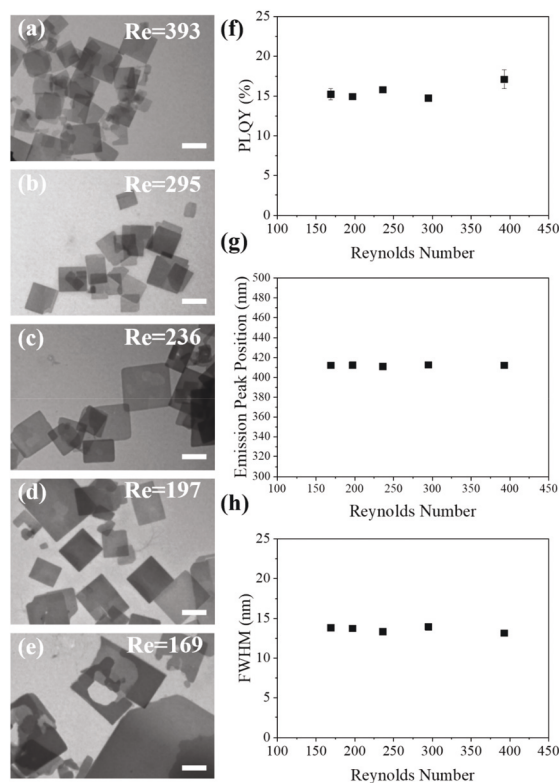


Fig. 4 (a–e) TEM images of  $(\text{PEA})_2\text{PbBr}_4$  NPLs synthesized in the flow reactor at varying toluene injection rates (from  $514$ – $1200 \text{ mL h}^{-1}$ ) with a constant precursor injection rate of  $5 \text{ mL h}^{-1}$ . All scale bars =  $2 \mu\text{m}$ . The effect of Reynolds Number on (f) PLQY, (g) emission peak position, and (h) FWHM of  $(\text{PEA})_2\text{PbBr}_4$  NPLs.

inner diameter of the PTFE tube. Generally, laminar flow is expected when  $Re < 2000$  and turbulent flow is yielded at  $Re > 2000$ . The  $Re$  for all flowrates in this trial did not exceed 2000 (the highest  $Re$  was 393; see ESI† for more details; Table S1†), suggesting that all experiments occurred in a laminar flow regime. This finding further enforces that, though the flowrates of each trial were different, nominal changes to their optical properties were observed because the nature of the flow was always laminar. In a similar study, altering  $Q_{\text{anti}}$  from  $6$ – $72 \text{ mL h}^{-1}$  was also found to affect little on the PL properties of flow reactor-synthesized  $\text{MAPbBr}_3$  NCs.<sup>55</sup> The lack of impact was ascribed to the finding that changing  $Q_{\text{anti}}$  had a limited influence on the concentration field of the system, as determined by finite element analysis.

It is notable that though many parameters were tuned throughout the trials, many of the optical properties of the  $(\text{PEA})_2\text{PbBr}_4$  NPLs remained relatively constant. FWHM and peak position of the PL were unchanged by altering the antisolvent composition, reactor tube length,  $Q_{\text{precursor}}$ , or  $Q_{\text{antisolvent}}$ . As seen in Fig. S14 and S15,† neither changing the antisolvents nor reactor tube length resulted in meaningfully altered peak position or FWHM. These stable optical properties are also in good agreement with those observed for changing  $Q_{\text{tol}}$ , as shown in Fig. 4g–h. The unchanged peak

position and FWHM of emission are consistent with the fact that all  $(\text{PEA})_2\text{PbBr}_4$  NPLs are monolayer thick. As the only available cation in the system is the monovalent bulky spacer PEA, any luminescent crystal formed is  $n = 1$   $(\text{PEA})_2\text{PbBr}_4$ . In addition, because of the nature of this material, all produced NPLs experience identical quantum confinement, ensuring a stable and constant emission.<sup>25</sup>

The optimized antisolvent,  $Q_{\text{precursor}}$ , reactor tube length, and  $Q_{\text{tot}}$  were then implemented to craft high-quality  $(\text{PEA})_2\text{PbBr}_4$  and  $(\text{PEA})_2\text{PbI}_4$  NPLs. Fig. 5a–d compares TEM images of NPLs produced from the optimized flow reactor as well as synthesized *via* conventional LARP batch synthesis. NPLs made from either strategy possess characteristic platelet morphology, while the NPLs synthesized from conventional LARP batch synthesis have a smaller average dimension. This decreased average size is due likely to the limited growth of NPL nuclei caused by the enhanced mixing of precursor solution with antisolvent *via* vigorous stirring. Conversely, in the microflow reactor, the laminar nature of the flow could allow a prolonged growth time of nuclei as discussed above and yield NPLs with larger dimensions. Fig. 5e–f present the UV-vis absorption and PL emission of flow-reactor-synthesized  $(\text{PEA})_2\text{PbBr}_4$  and  $(\text{PEA})_2\text{PbI}_4$  NPLs, respectively. The emission peaks of 410 nm for  $(\text{PEA})_2\text{PbBr}_4$ <sup>56,57</sup> and 520 nm for  $(\text{PEA})_2\text{PbI}_4$ <sup>40</sup> are in good agreement with those reported for NPLs made *via* conventional LARP. The absorption peaks are similarly consistent with previous reported results. It is worth noting that the average absolute PLQYs (measured *via* an integrating sphere) of  $(\text{PEA})_2\text{PbBr}_4$  (18.5%) and  $(\text{PEA})_2\text{PbI}_4$  (1.5%) NPLs formed in the flow reactor at optimized conditions are comparable (or better) to those of  $(\text{PEA})_2\text{PbBr}_4$  (with reported values ranging from 5–24.8%)<sup>56,57</sup> and  $(\text{PEA})_2\text{PbI}_4$  (~1%)<sup>40</sup> NPLs synthesized by LARP batch synthesis.<sup>20</sup> The average PLQY, FWHM, and emission peak position of  $(\text{PEA})_2\text{PbI}_4$  NPLs created in an optimized flow reactor ( $l = 15$  cm,  $Q_{\text{tot}} = 1200$  mL  $\text{h}^{-1}$ ) with  $Q_{\text{precursor}}$  ranging from 5–30 mL  $\text{h}^{-1}$  are summarized in Fig. S16.† Atomic force microscopy was performed to verify the monolayer nature of the  $(\text{PEA})_2\text{PbBr}_4$  NPLs made with the

optimized parameters (Fig. S17†). The observed thickness of ~2 nm (Fig. S17b†) is in good agreement with previous study that reported the monolayer thickness of  $(\text{PEA})_2\text{PbBr}_4$  to be 1.75 nm.<sup>66</sup>

The effect of precursor solution concentration was then investigated. To accomplish this, the precursor solution concentration was doubled (from 0.02 M  $\text{PbBr}_2$  and 0.04 M  $\text{PEABr}$  to 0.04 M  $\text{PbBr}_2$  and 0.08 M  $\text{PEABr}$  in DMF), and the optimized flow parameters (toluene antisolvent,  $Q_{\text{tot}} = 1200$  mL  $\text{h}^{-1}$ ,  $Q_{\text{precursor}} = 5$  mL  $\text{h}^{-1}$ , 15 cm reactor tube) were used. Fig. S18† shows TEM images of NPLs synthesized with concentrated precursor solutions at  $Q_{\text{precursor}}$  ranging from 5–30 mL  $\text{h}^{-1}$ . No obvious trend can be seen in their morphology, with each  $Q_{\text{precursor}}$  resulting in NPLs with highly variable sizes. The PLQY of NPLs made from concentrated precursors was found to remain at a relatively constant value of ~9% regardless of precursor injection rate (Fig. S19a†). This value is significantly lower than that of the more dilute sample, which displayed a highest PLQY of ~18%. Interestingly, the lowest PLQY from the dilute samples (~11%) occurred at the highest  $Q_{\text{precursor}}$ . The relative similarity between the constant PLQY of the concentrated samples (~9%) and that highest  $Q_{\text{precursor}}$  of the dilute sample (~11%) could suggest that a critical ratio of precursor to antisolvent exists, beyond which PLQY will remain constant. At this critical ratio, there is potentially not sufficient toluene to spur crystallization of all perovskite precursors, leading to crystals with poor PL performance. Moreover, the emission peak position and FWHM were found to be relatively unaffected by changing the precursor concentration (Fig. S19b and c†). This is in good agreement with previous findings which have shown peak position and FWHM to be relatively stable throughout a variety of parameter tuning.

Production rate (mass per time) is a key metric to evaluate the viability of any continuous production system. Determining the production rate of legacy batch synthesis strategies is difficult, because the time component is highly dependent on the rate at which batches are switched. As an estimate, we assumed that lab-scale batch synthesis of perovskite NPLs takes on average 60 s per batch, not including purification or cleaning of the reactors. Using this approximation, we estimated the production rate of batch synthesis to be 0.0185 g  $\text{h}^{-1}$  (see full calculation in ESI†). We then calculated the production rate of the flow reactor to be 0.1542 g  $\text{h}^{-1}$  (see ESI†). These calculations demonstrate well that our flow reactor enables a greater than eight times increase in the production rate of 2D RP perovskite NPLs. We also note that all samples yielded in the flow reactor were characterized without purification, which avoids the need for an additional and potentially costly step that could hinder commercial applications.

## Conclusion

In summary, we demonstrated that a flow reactor is capable of continuously producing both  $(\text{PEA})_2\text{PbBr}_4$  and  $(\text{PEA})_2\text{PbI}_4$  NPLs with properties comparable to those of NPLs previously

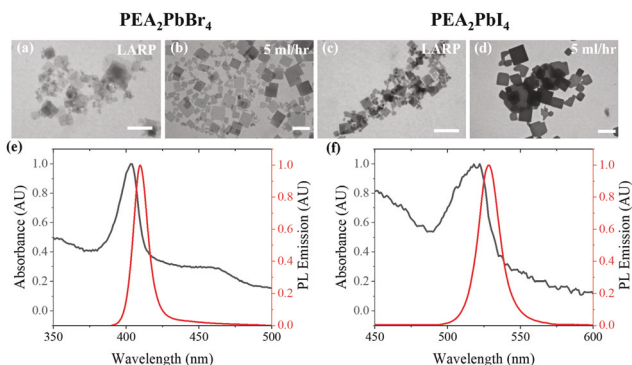


**Fig. 5** TEM images of (a) and (c) LARP control and (b) and (d) flow reactor (1200 mL  $\text{h}^{-1}$  toluene and 5 mL  $\text{h}^{-1}$  precursor)  $(\text{PEA})_2\text{PbBr}_4$  and  $(\text{PEA})_2\text{PbI}_4$  NPLs, respectively. All scale bars = 2  $\mu\text{m}$ . (e)–(f) UV-vis absorbance and PL of (e)  $(\text{PEA})_2\text{PbBr}_4$  and (f)  $(\text{PEA})_2\text{PbI}_4$  NPLs, respectively.

reported from batch synthesis. The selection of antisolvent (particularly its polarity) was witnessed to drastically affect the properties of the NPLs, with lower polarity solvents achieving better PLQY due to the absence of degradation of NPLs often caused by polar solvents. Furthermore, a moderate decrease in PLQY was observed as reactor tube length increased, which may be due to longer tubes resulting in a longer residence time that promotes interaction between DMF and the NPLs and thus the NPL degradation. In addition, altering the flow-rate of antisolvent was not found to meaningfully affect any of the tested optical properties (e.g., PLQY, FWHM, peak position), which can be attributed to the laminar flow characteristic at all injection rates. Antisolvent flowrate was, however, found to affect NPL morphology, with higher flowrates resulting in smaller and more monodisperse NPLs. A trend of higher PLQY with lower flowrates of precursor solution was noted for the toluene samples and was attributed to a relatively lower concentration of DMF in the final product solution, leading to less degradation of as-formed NPLs. Nearly all samples displayed a constant emission peak position and FWHM, correlating well with the nature of the highly quantum-confined 2D RP perovskite structure. Our systematic study displayed that 2D RP perovskite NPLs with competitive PL properties (i.e., PLQY, FWHM, and emission peak position) can be produced at rates eight times greater than that of traditional batch synthesis. This scaling-up represents a viable and crucial step towards far-reaching commercial applications of 2D RP perovskite NPLs. Insights gleaned from this investigation can be exercised to scale up production of other perovskite materials, including Dion–Jacobson (DJ) perovskites and RP perovskites where  $n > 1$ .

## Conflicts of interest

There are no conflicts to declare.

## Acknowledgements

This work is supported by the National Science Foundation (CMMI 1914713) and the Defense Threat Reduction Agency (DTRA) (HDTRA1-18-1-0004).

## References

- C.-H. Lu, G. V. Biesold-McGee, Y. Liu, Z. Kang and Z. Lin, *Chem. Soc. Rev.*, 2020, **49**, 4953–5007.
- H. Huang, M. I. Bodnarchuk, S. V. Kershaw, M. V. Kovalenko and A. L. Rogach, *ACS Energy Lett.*, 2017, **2**, 2071–2083.
- S. Gonzalez–Carrero, L. Francés–Soriano, M. González–Béjar, S. Agouram, R. E. Galian and J. Pérez–Prieto, *Small*, 2016, **12**, 5245–5250.
- S. Gonzalez–Carrero, R. E. Galian and J. Pérez–Prieto, *J. Mater. Chem. A*, 2015, **3**, 9187–9193.
- L. C. Schmidt, A. Pertegás, S. González–Carrero, O. Malinkiewicz, S. Agouram, G. Minguez Espallargas, H. J. Bolink, R. E. Galian and J. Pérez–Prieto, *J. Am. Chem. Soc.*, 2014, **136**, 850–853.
- F. Liu, Y. Zhang, C. Ding, S. Kobayashi, T. Izuishi, N. Nakazawa, T. Toyoda, T. Ohta, S. Hayase and T. Minemoto, *ACS Nano*, 2017, **11**, 10373–10383.
- S. Bai, Z. Yuan and F. Gao, *J. Mater. Chem. C*, 2016, **4**, 3898–3904.
- M. V. Kovalenko, L. Protesescu and M. I. Bodnarchuk, *Science*, 2017, **358**, 745–750.
- L. Protesescu, S. Yakunin, M. I. Bodnarchuk, F. Krieg, R. Caputo, C. H. Hendon, R. X. Yang, A. Walsh and M. V. Kovalenko, *Nano Lett.*, 2015, **15**, 3692–3696.
- M. He, X. Pang, X. Liu, B. Jiang, Y. He, H. Snaith and Z. Lin, *Angew. Chem., Int. Ed.*, 2016, **128**, 4352–4356.
- M. Ye, C. He, J. Iocozzia, X. Liu, X. Cui, X. Meng, M. Rager, X. Hong, X. Liu and Z. Lin, *J. Phys. D: Appl. Phys.*, 2017, **50**, 373002.
- M. He, B. Li, X. Cui, B. Jiang, Y. He, Y. Chen, D. O’Neil, P. Szymanski, M. A. Ei-Sayed, J. Huang and Z. Lin, *Nat. Commun.*, 2017, **8**, 16045.
- F.-W. Liu, G. Biesold, M. Zhang, R. Lawless, J.-P. Correa-Baena, Y.-L. Chueh and Z. Lin, *Mater. Today*, 2021, **43**, 185–197.
- Y. Chang, Y. J. Yoon, G. Li, E. Xu, S. Yu, C.-H. Lu, Z. Wang, Y. He, C. H. Lin and B. K. Wagner, *ACS Appl. Mater. Interfaces*, 2018, **10**, 37267–37276.
- S. Pan, Y. Chen, Z. Wang, Y.-W. Harn, J. Yu, A. Wang, M. J. Smith, Z. Li, V. V. Tsukruk and J. Peng, *Nano Energy*, 2020, **77**, 105043.
- S. Pan, H. Zou, A. C. Wang, Z. Wang, J. Yu, C. Lan, Q. Liu, Z. L. Wang, T. Lian and J. Peng, *Angew. Chem., Int. Ed.*, 2020, **59**, 14942–14949.
- C. Lan, H. Zou, L. Wang, M. Zhang, S. Pan, Y. Ma, Y. Qiu, Z. L. Wang and Z. Lin, *Adv. Mater.*, 2020, **32**, 2005481.
- X. Hong, T. Ishihara and A. Nurmikko, *Phys. Rev. B: Condens. Matter Mater. Phys.*, 1992, **45**, 6961.
- C. C. Stoumpos, D. H. Cao, D. J. Clark, J. Young, J. M. Rondinelli, J. I. Jang, J. T. Hupp and M. G. Kanatzidis, *Chem. Mater.*, 2016, **28**, 2852–2867.
- M. C. Weidman, M. Seitz, S. D. Stranks and W. A. Tisdale, *ACS Nano*, 2016, **10**, 7830–7839.
- H. Tsai, W. Nie, J.-C. Blancon, C. C. Stoumpos, R. Asadpour, B. Harutyunyan, A. J. Neukirch, R. Verduzco, J. J. Crochet and S. Tretiak, *Nature*, 2016, **536**, 312–316.
- J. Cherusseri, S. J. Varma, B. Pradhan, J. Li, J. Kumar, E. Barrios, M. Z. Amin, A. Towers, A. Gesquiere and J. Thomas, *Nanoscale*, 2020, **12**, 10072–10081.
- N. Wang, L. Cheng, R. Ge, S. Zhang, Y. Miao, W. Zou, C. Yi, Y. Sun, Y. Cao and R. Yang, *Nat. Photonics*, 2016, **10**, 699–704.
- M. Safdari, P. H. Svensson, M. T. Hoang, I. Oh, L. Kloo and J. M. Gardner, *J. Mater. Chem. A*, 2016, **4**, 15638–15646.
- J. A. Sichert, Y. Tong, N. Mutz, M. Vollmer, S. Fischer, K. Z. Milowska, R. García Cortadella, B. Nickel, C. Cardenas-Daw and J. K. Stolarczyk, *Nano Lett.*, 2015, **15**, 6521–6527.

- 26 Y. Liang, Q. Shang, Q. Wei, L. Zhao, Z. Liu, J. Shi, Y. Zhong, J. Chen, Y. Gao and M. Li, *Adv. Mater.*, 2019, **31**, 1903030.
- 27 D. Parobek, B. J. Roman, Y. Dong, H. Jin, E. Lee, M. Sheldon and D. H. Son, *Nano Lett.*, 2016, **16**, 7376–7380.
- 28 A. De, S. Das, N. Mondal and A. Samanta, *ACS Mater. Lett.*, 2019, **1**, 116–122.
- 29 T. Ahmed, S. Seth and A. Samanta, *Chem. Mater.*, 2018, **30**, 3633–3637.
- 30 A. De, N. Mondal and A. Samanta, *Nanoscale*, 2017, **9**, 16722–16727.
- 31 Z. Guo, X. Wu, T. Zhu, X. Zhu and L. Huang, *ACS Nano*, 2016, **10**, 9992–9998.
- 32 Y. N. Chen, Y. Sun, J. J. Peng, J. H. Tang, K. B. Zheng and Z. Q. Liang, *Adv. Mater.*, 2018, **30**, 1703487.
- 33 G. Xing, B. Wu, X. Wu, M. Li, B. Du, Q. Wei, J. Guo, E. K. Yeow, T. C. Sum and W. Huang, *Nat. Commun.*, 2017, **8**, 1–9.
- 34 H. Z. Wang, C. Fang, H. M. Luo and D. H. Li, *J. Semicond.*, 2019, **40**, 041901.
- 35 Y. Liao, H. Liu, W. Zhou, D. Yang, Y. Shang, Z. Shi, B. Li, X. Jiang, L. Zhang and L. N. Quan, *J. Am. Chem. Soc.*, 2017, **139**, 6693–6699.
- 36 C. C. Stoumpos, C. M. M. Soe, H. Tsai, W. Nie, J.-C. Blancon, D. H. Cao, F. Liu, B. Traoré, C. Katan and J. Even, *Chem*, 2017, **2**, 427–440.
- 37 I. C. Smith, E. T. Hoke, D. Solis-Ibarra, M. D. McGehee and H. I. Karunadasa, *Angew. Chem., Int. Ed.*, 2014, **126**, 11414–11417.
- 38 M. Yuan, L. N. Quan, R. Comin, G. Walters, R. Sabatini, O. Voznyy, S. Hoogland, Y. Zhao, E. M. Beauregard and P. Kanjanaboos, *Nat. Nanotechnol.*, 2016, **11**, 872–877.
- 39 X. Yang, X. Zhang, J. Deng, Z. Chu, Q. Jiang, J. Meng, P. Wang, L. Zhang, Z. Yin and J. You, *Nat. Commun.*, 2018, **9**, 1–8.
- 40 D. Yu, F. Cao, Y. Gu, Z. Han, J. Liu, B. Huang, X. Xu and H. Zeng, *Nano Res.*, 2021, **14**, 1210–1217.
- 41 D. Yu, F. Cao, Y. Shen, X. Liu, Y. Zhu and H. Zeng, *J. Phys. Chem. Lett.*, 2017, **8**, 2565–2572.
- 42 Z. Tan, Y. Wu, H. Hong, J. Yin, J. Zhang, L. Lin, M. Wang, X. Sun, L. Sun and Y. Huang, *J. Am. Chem. Soc.*, 2016, **138**, 16612–16615.
- 43 I. Levchuk, A. Osvet, X. Tang, M. Brandl, J. D. Perea, F. Hoegl, G. J. Matt, R. Hock, M. Batentschuk and C. J. Brabec, *Nano Lett.*, 2017, **17**, 2765–2770.
- 44 J. Song, J. Li, X. Li, L. Xu, Y. Dong and H. Zeng, *Adv. Mater.*, 2015, **27**, 7162–7167.
- 45 Y. Pu, F. Cai, D. Wang, J.-X. Wang and J.-F. Chen, *Ind. Eng. Chem. Res.*, 2018, **57**, 1790–1802.
- 46 H. Tang, Y. He, B. Li, J. Jung, C. Zhang, X. Liu and Z. Lin, *Nanoscale*, 2015, **7**, 9731–9737.
- 47 X. Liang, R. W. Baker, K. Wu, W. Deng, D. Ferdani, P. S. Kubiak, F. Marken, L. Torrente-Murciano and P. J. Cameron, *React. Chem. Eng.*, 2018, **3**, 640–644.
- 48 G. Niu, A. Ruditskiy, M. Vara and Y. Xia, *Chem. Soc. Rev.*, 2015, **44**, 5806–5820.
- 49 R. W. Epps, K. C. Felton, C. W. Coley and M. Abolhasani, *Lab Chip*, 2017, **17**, 4040–4047.
- 50 K. Ma, X.-Y. Du, Y.-W. Zhang and S. Chen, *J. Mater. Chem. C*, 2017, **5**, 9398–9404.
- 51 I. Lignos, S. Stavrakis, G. Nedelcu, L. Protesescu, A. J. deMello and M. V. Kovalenko, *Nano Lett.*, 2016, **16**, 1869–1877.
- 52 R. M. Maceiczkyk, K. Dümbgen, I. Lignos, L. Protesescu, M. V. Kovalenko and A. J. deMello, *Chem. Mater.*, 2017, **29**, 8433–8439.
- 53 Y. H. Song, S. H. Choi, W. K. Park, J. S. Yoo, S. B. Kwon, B. K. Kang, S. R. Park, Y. S. Seo, W. S. Yang and D. H. Yoon, *Sci. Rep.*, 2018, **8**, 1–6.
- 54 C. Zhang, W. Luan, Y. Yin and F. Yang, *Beilstein J. Nanotechnol.*, 2017, **8**, 2521–2529.
- 55 C. Li, B. Ding, L. Zhang, K. Song and S. Tao, *J. Mater. Chem. C*, 2019, **7**, 9167–9174.
- 56 X. Gao, X. Shen, D. Xue, X. Li, P. Lu, M. Lu, C. Li, W. Y. William and X. Bai, *Mater. Chem. Front.*, 2021, **5**, 937–943.
- 57 S. Zeng, S. Shi, S. Wang and Y. Xiao, *J. Mater. Chem. C*, 2020, **8**, 1319–1325.
- 58 L. Zhang, T. Jiang, C. Yi, J. Wu, X.-K. Liu, Y. He, Y. Miao, Y. Zhang, H. Zhang and X. Xie, *J. Phys. Chem. Lett.*, 2019, **10**, 3171–3175.
- 59 S. Yang, W. Niu, A. L. Wang, Z. Fan, B. Chen, C. Tan, Q. Lu and H. Zhang, *Angew. Chem., Int. Ed.*, 2017, **56**, 4252–4255.
- 60 C. Reichardt and T. Welton, *Solvents and solvent effects in organic chemistry*, John Wiley & Sons, 2011.
- 61 F. Zhang, S. Huang, P. Wang, X. Chen, S. Zhao, Y. Dong and H. Zhong, *Chem. Mater.*, 2017, **29**, 3793–3799.
- 62 Y. Tang, N. Yan, Z. Wang, H. Yuan, Y. Xin and H. Yin, *J. Alloys Compd.*, 2019, **773**, 227–233.
- 63 B. J. Kim, D. H. Kim, S. L. Kwon, S. Y. Park, Z. Li, K. Zhu and H. S. Jung, *Nat. Commun.*, 2016, **7**, 1–9.
- 64 D. Jeevarathinam, A. Gupta, B. Pitchumani and R. Mohan, *Chem. Eng. J.*, 2011, **173**, 607–611.
- 65 J. Sui, J. Yan, D. Liu, K. Wang and G. Luo, *Small*, 2020, **16**, 1–23.
- 66 K. Shibuya, M. Koshimizu, F. Nishikido, H. Saito and S. Kishimoto, *Acta Crystallogr., Sect. E: Struct. Rep. Online*, 2009, **65**, m1323–m1324.